Efficient synthesis of H_2O_2 *via* oxygen reduction over PANI driven by kinetics regulation of carbon dots

Yunjie Zhou [a], Xiaoqing Gu [a], Jie Wu [a], Hui Huang [a], Mingwang Shao [a], Yang Liu [a,*], Zhenhui Kang [a,b,**]

[a] *Institute of Functional Nano and Soft Materials (FUNSOM), Jiangsu Key Laboratory for Carbon-Based Functional Materials and Devices, Soochow University, 215123 Suzhou, China*
[b] *Macao Institute of Materials Science and Engineering (MIMSE), MUST−SUDA Joint Research Center for Advanced Functional Materials, Macau University of Science and Technology, Taipa 999078, Macao,China*

ARTICLE INFO

ABSTRACT

Electrocatalytic two-electron ($2e^-$) oxygen reduction reaction (ORR) is a promising method to realize the sustainable production of H_2O_2. However, the $4e^-$ pathway competes with $2e^-$ ORR, presenting a challenge to the design of highly selective, low-cost catalysts. In addition to the design of active sites, the regulation on electrocatalytic kinetics is another strategy to get ideal $2e^-$ ORR route. Here, cobalt doped carbon dots (CDs-Co) were used to regulate the electron transport kinetics on polyaniline (PANI) by constructing p-n heterojunction. The electron transfer kinetics and oxygen molecular activation process on PANI/CDs-Co were studied and analyzed using the transient photo-induced voltage (TPV) and pulse voltage-induced current (PVC) technologies, respectively. These results show that CDs-Co not only reduces the over-potential of oxygen molecular activation, but also reduces the transient electron concentration on PANI, which effectively improves the selectivity and activity of H_2O_2 production *via* ORR. The obtained PANI/CDs-Co-2 shows a H_2O_2 selectivity nearly 100.0% higher than that of PANI (76.3%). And it exhibits a H_2O_2 productivity of 3.5 mol g_{cat}^{-1} h^{-1} at 0 V *vs*. RHE tested by gas diffusion electrode device. This work provides new insights for the design of $2e^-$ ORR catalysts and the study of electrocatalytic kinetics.

1. Introduction

Hydrogen peroxide (H_2O_2), as an important industrial chemical and a green oxidant, has been widely applied from chemical synthesis to potential energy carrier and environmental treatment [1,2]. Currently, most of H_2O_2 is industrially produced *via* the anthraquinone process, which accompanied with energy-intensive, high cost and negative environmental impacts [3,4]. Recently, the electrochemical synthesis of H_2O_2 *via* a two-electron ($2e^-$) oxygen reduction reaction (ORR) pathway offers an attractive route, aiming to enable portable, environmentally friendly, on-demand synthesis of H_2O_2 [5,6]. However, the $4e^-$ ORR pathway toward H_2O competes with the $2e^-$ pathway and is more thermodynamically favorable [7]. In recent decades, tremendous efforts have been put into the design of $2e^-$ ORR catalysts, and noble metal alloys such as Pd−Hg, Pt−Hg and Au−Pd have been proved to be

efficient catalysts for the production of H_2O_2 [8,9]. These rarity and high cost of these catalysts prevent their practical application. Recently, a series of non-noble metal-based catalysts have been reported, such as carbon supported metal single-atom catalysts [10–12], transition metal dichalcogenides [13] and metal-free carbon materials [14–16]. Nevertheless, the development of high-performance and low-cost electrocatalyst remains a tremendous challenge [17,18].

In addition to the design of active sites, the regulation on electron transmission, namely, the electrocatalytic kinetics, is another strategy to get ideal $2e^-$ ORR pathway. In particular, reducing the amount of charge supplied by the catalytic site to oxygen molecules can effectively weaken the strong adsorption of oxygen molecules during the synthesis of H_2O_2, so as to maintain the O-O bond [19–22]. While, it is paid few attentions due to the limitations of classical experimental technology and electrochemical methodology. Different from adjusting the binding energy

---

of catalysts to intermediate OOH* or adjusting the adsorption configuration of active species to achieve efficient $2e^-$ ORR selectivity [23–26], we turn our attention to the regulation of electrocatalytic kinetics, an important but rarely noticed step in the electrocatalytic process due to the difficulty in catalyst design and the lack of characterization technology. Carbon dots (CDs) as a cocatalyst, can play an unique role in regulating the electron transport process, acting as an electron acceptor and electron donor and having electron sink effect that can change the local charge distribution [27–32]. Besides, transient photo-induced voltage (TPV) technology developed by our group can be used to investigate the electron transport kinetics and has been successfully used in other catalytic studies [27,33–35]. On the other hands, pulse voltage-induced current (PVC) technology was applied for the first time to study the ORR process driven by applied bias, especially the effect of over-potential on the activation of O_2 molecular.

Polyaniline (PANI), as a conducting polymer, has been widely employed in various fields because of its high conductivity and stability, easy synthesis, low cost, high hydrophilic property and environmentally friendliness. It has attracted much interest as a support in hybrid materials, such as PANI supported $Co(OH)_2$ [36], Pt/CeO_2 [37], CoP [38] and hierarchically structured metals [39], which have excellent performance in electrocatalysis. However, PANI is rarely used as a catalyst directly, and it is usually annealed at high temperature to obtain high-efficiency catalysts, which requires additional processing and cannot maintain its original advantages [40,41]. PANI shows promising application as electrocatalyst, but limited in selectivity [42], and then how to make PANI with higher H_2O_2 selectivity is a challenge.

Herein, we reported the use of Co doped CDs (CDs−Co) as a cocatalyst and TPV and PVC as observation tools to regulate the electron transport kinetics occurred on PANI. PANI/CDs-Co heterojunction was constructed to investigate the $2e^-$ ORR performance. The PANI/CDs−Co− 2 delivers a high H_2O_2 selectivity close to 100% at $0.2 - 0.5$ V, which is much higher than PANI of 76.3%. Besides, the PANI/CDs−Co− 2 achieved a H_2O_2 productivity of 3.5 mol g_{cat}^{-1} h^{-1} at 0 V *vs.* RHE and a Faraday efficiency about 86.5%, surpassing most of the reported catalysts in alkaline electrolyte. TPV results show that PANI and CDs−Co form a heterojunction and the electron rapidly transfer from PANI to CDs−Co, resulting in a decrease in the concentration of transient charge at the PANI site and a higher H_2O_2 selectivity. PVC results show that CDs−Co can effectively reduce the over−potential required for O_2 activation. This work provides new ideas for the design and mechanism of efficient $2e^-$ ORR catalysts.

2. Experimental section

2.1. Synthesis of CDs−Co

$Co(acac)_2$ was loaded into a ceramic boat and placed in the center of a quartz tube of a tube furnace. The $Co(acac)_2$ was calcined at 300 ℃ for 2 h with a heating rate of 5 ℃ min^{-1} under N_2 atmosphere. Then, 50 mL anhydrous methanol was added to extract CDs−Co from the product. The obtained suspension was ultrasonized for 30 min, and centrifuged at the speed of 16,500 rpm for 30 min to take the supernatant. The brown supernatant was filtered with 0.22 μm nylon syringe filters to remove carbon fragments. The obtained solution was mixed with 100 mL HCl (0.1 M), and ultrasound was performed for 2 h to remove cobalt oxide. The solution was then dialyzed for three days. CDs−Co powder was obtained by drying the resulting solution in 60 ℃ vacuum oven.

2.2. Synthesis of PANI and PANI/CDs−Co

Under the ice−water bath conditions, 69 μL of aniline was dissolved in 10 mL of ultrapure water. Then, 0.1 mL HCl (0.1 M) and 0.18 g of $(NH_4)_2S_2O_8$ were added to the above solution. Then the reactants were stirred continuously for 24 h. Next, the resulting solution was washed with ultrapure water and ethanol several times until the supernatant was

almost clear and transparent. The precipitate obtained after centrifugation was collected and dried in a 60 ℃ vacuum oven. The synthesis method of PANI/CDs−Co composites is similar, different amount (1 mg, 2 mg, 3 mg, 4 mg) of CDs−Co were added to the solution in the first step.

3. Results and discussion

3.1. Catalysts preparation and characterizations

PANI was synthesized from aniline and ammonium persulfate in ice bath, and PANI/CDs−Co was obtained by adding CDs−Co before polymerization (Fig. 1a). The CDs−Co was synthesized by pyrolysis Co $(acac)_2$ at 300 °C in N_2 atmosphere for 2 h, which was the optimum carbonation temperature to form CDs (Fig. S1). Transmission electron microscopy (TEM) and high resolution transmission electron microscope (HRTEM) images show a lateral size distribution of $2 - 8$ nm and a lattice spacing of 0.21 nm, matching with the (100) interplanar spacing of graphite [43]. Aberration corrected high angle annular dark field scanning transmission electron microscopy (HAADF−STEM) was used to observe the distribution of Co at CDs. As shown in Fig. 1c, atom scale bright spots represent the location of Co atoms that are distributed on the surface of CDs, and there is no characteristic peak corresponding to $Co(acac)_2$, metallic Co or other cobalt derived matter can be observed in the X − ray diffraction (XRD) pattern (Fig. S2) of CDs−Co, indicating that Co element chelated by acetyl acetone are successfully retained in the CDs framework during carbonization. The content of the Co element loaded on CDs-Co is about 0.57 wt% tested by Inductively Coupled Plasma Mass Spectrometry (ICP-MS). As shown in Figs. 1d and S3, the scanning electron microscope (SEM) images reveal that PANI and PANI in the composite are composed of nanofibers with an average diameter of 90 nm. XRD patterns (Fig. S4) also show that the structure of PANI is basically unchanged, indicating that the introduction of CD−Co has no effect on the polymerization morphology of aniline. Besides, TEM (Fig. 1e) and HRTEM images (Fig. 1f) show that a large number of uniformly distributed CDs−Co can be observed on PANI, which is obviously different from the TEM and HRTEM images of pure PANI (Fig. S5). Moreover, the element mapping of PANI/CDs−Co− 2 is shown in Fig. 1g, where C, N O, Co elements are evenly distributed on the nanofibers of PANI. The content of the Co element in PANI/CDs−Co− 2 is about 0.04 wt% tested by ICP-MS, so the content of CDs-Co loaded on PANI/CDs−Co− 2 is about 7.5 wt%. Meanwhile, similar results are also obtained on PANI, but without signal of Co (Fig. S6).

By comparing the FT−IR spectra of $Co(acac)_2$ and CDs−Co (Fig. 2a), it can be found that peaks at 2975, 1465, 1396, 1259, 934 and 770 cm^{-1} associated with the vibration of $-CH_2 -$, C=O, $-CH_3$ and C−H were replaced by the peaks at 1560, 1410, 1167 and 1035 cm^{-1} belonging to C=O, −OH, C−O−C and C−O. Furthermore, the peak at 674 cm^{-1} attributed to Co−O was retained [44]. This result indicates that Co $(acac)_2$ is completely condensed into CDs after carbonization, and the original chelated Co atoms are retained in the form of Co−O. The X − ray photoelectron spectroscopy (XPS) was used to obtain the detail element information of sample surface. Fig. 2b shows the Co 2p spectrum of CDs−Co, in which two peaks at 780.6 and 796.2 eV can be attributed to the $2p_{3/2}$ and $2p_{1/2}$ orbitals of Co^{2+} species, respectively [45]. The fine detail of CDs−Co at the atomic level was further investigated by synchrotron X − ray absorption spectroscopy (XAS). Fig. 2c shows that the absorption edge position of CDs−Co is located at 7726 eV, which is nearly the same position of CoO [46]. Furthermore, extended X − ray absorption fine structure (EXAFS) analysis was used to probe the possible bonding between the Co and light elements (C/O) in CDs−Co by wavelet transform (WT) and Fourier transform. As shown in Fig. 2d, The EXAFS signal of CDs−Co in the R space occupies characteristic peak (≈1.5 Å), which can be assigned to the coordination of Co−C/O, and no Co−Co coordination peak (≈2.2 Å) can be detected. Meanwhile, the fine structure of PANI/CDs−Co− 2 was also investigated by N K−edge XANES spectrum. As shown in Fig. 2e, there are
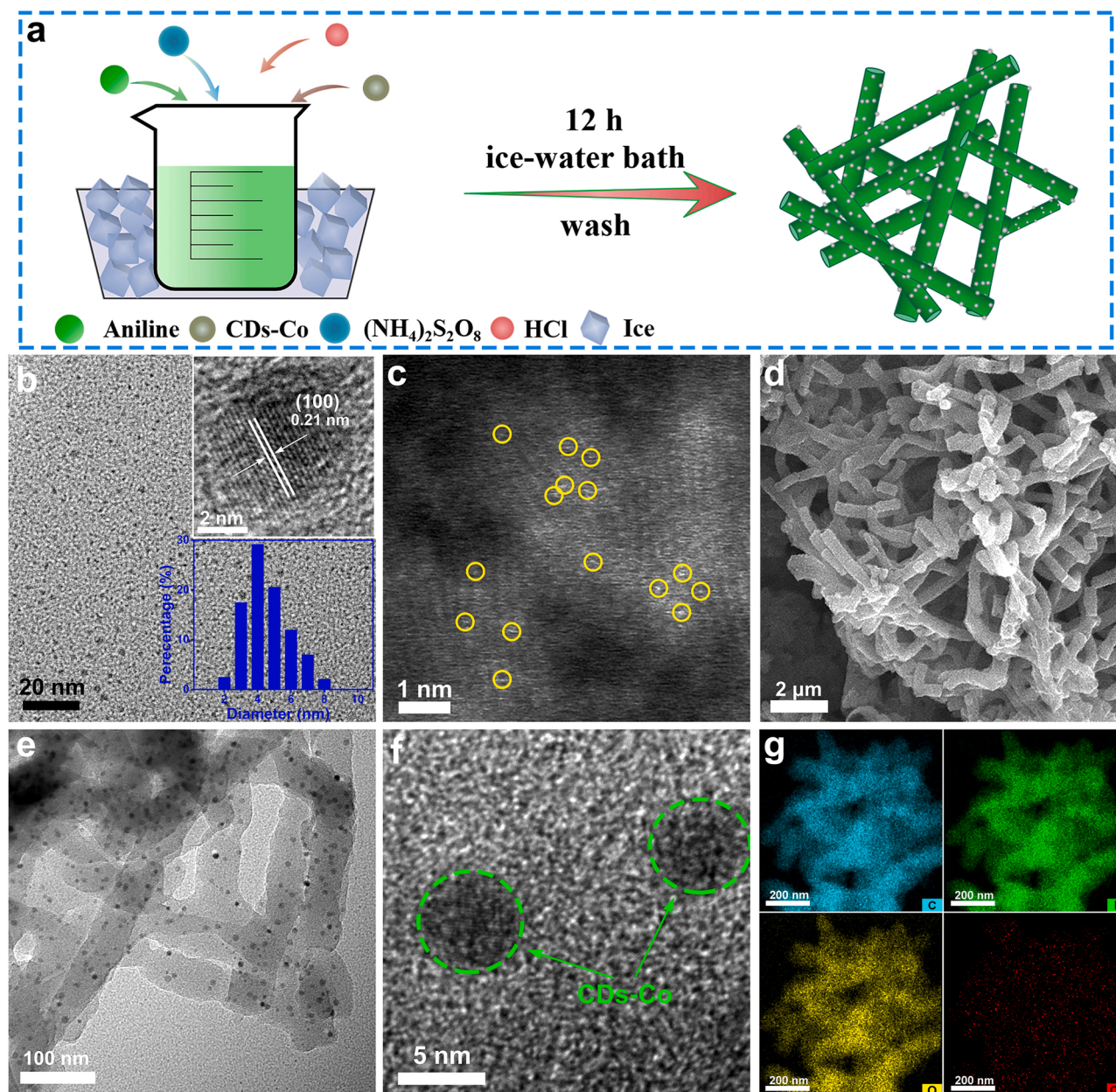
Fig. 1. Schematic diagram of synthesis and morphology structure. (a) The schematic diagram of the synthesis of PANI/CDs−Co− 2. (b) TEM and HRTEM images of CDs−Co. (c) HAADF−STEM image of distributed Co atoms in CDs−Co. Yellow circles in (c) indicate typical Co atoms. (d) SEM image of PANI/CDs−Co− 2. (e) TEM images of PANI and PANI/CDs−Co− 2. (f) HRTEM image of PANI/CDs−Co− 2. (g) Element mapping images of PANI/CDs−Co− 2.

three peaks at 397.7, 399.1 and 402.7 eV, belonging to imine nitrogen atoms, radical cation nitrogen atoms and amine nitrogen atoms, respectively, which are generally close to the emeraldine salt situation of PANI [47]. The C $K-$edge spectrum (Fig. 2f) of PANI/CDs−Co− 2 shows peaks at approximately 285.5 eV, 286.9 eV and 288.4 eV. The peak at 285.5 eV can be attributed to the π * antibonding state of sp^2 (C=C) sites in a conjugated carbon ring structure. The peaks located at 286.9 eV and 288.4 eV are related to the C 1 s$\rightarrow\pi$ * transitions induced by the presence of C−N and C=O, respectively [48].

3.2. Electrocatalytic $2e^-$ ORR performance of catalysts

The ORR electrochemical performance was evaluated based on a typical three electrode system in an O_2 −saturated 0.1 M KOH electrolyte, and the selectivity of H_2O_2 was measured using a rotating ring−disk electrode (RRDE) at 1600 rpm. The collection efficiency of RRDE

was calibrated to be 0.37 (Fig. S7). Fig. 3a shows the polarization curves for CDs−Co, PANI, and PANI/CDs−Co− 2, with the oxygen reduction current density measured on the disk electrode and the H_2O_2 oxidation current on the Pt ring electrode. The performance of catalysts with different content of CDs−Co are shown in Fig. S8. Among all the catalysts, PANI/CDs−Co− 2 exhibited the highest oxygen reduction current (1.9 mA cm^{-2}) and most positive onset potential 0.68 V *vs.* RHE (determined at the current density of 0.1 mA cm^{-2}) at the disk electrode, indicating its highest ORR activity. Fig. 3b shows the LSV curves of PANI/CDs−Co− 2 at various rotational speeds (800, 1200, 1600, 2000 and 2400 rpm), indicating that the current rises with the increase of the electrode rotating speed. The corresponding Koutecky–Levich (K–L) plots at 0.1, 0.2, 0.3, and 0.4 V are shown inset Fig. 3b, and the electron transfer number (n) per O_2 molecule is calculated to be about 2.02. Furthermore, the electron transfer number and H_2O_2 selectivity are also calculated from RRDE curves and plotted in Fig. 3c and d.
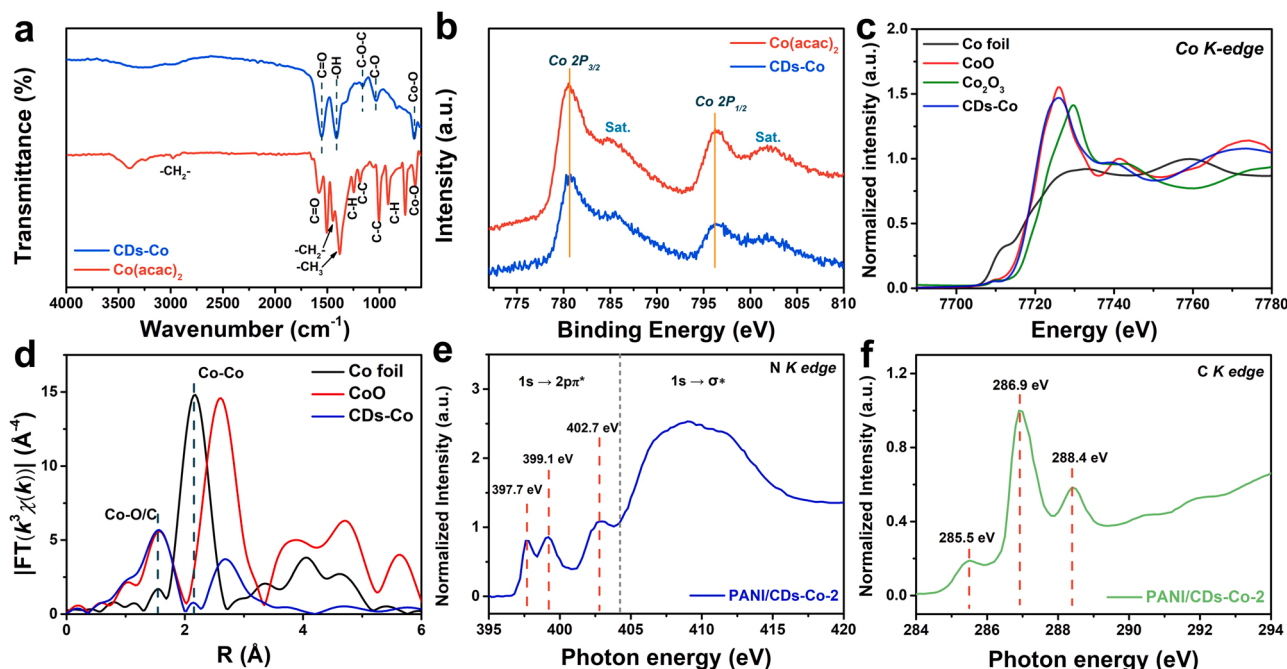
Fig. 2. Structural characterization of CDs-Co and PANI/CDs-Co-2. (a) FTIR spectra of CDs−Co and Co(acac)$_2$. (b) The high−resolution XPS spectra of Co 2p of CDs−Co and Co(acac)$_2$. (c) X − ray absorption near−edge structure (XANES) spectra of Co foil, CoO, Co$_2$O$_3$ and CDs−Co. (d) Fourier transform (FT) EXAFS spectra at the Co K−edge of CDs−Co, Co foil and CoO. (e, f) N and C K−edge XANES spectra of PANI/CDs−Co− 2.

CDs−Co possesses the highest electron transfer number (3.90) and the lowest H$_2$O$_2$ selectivity (3.4%) at 0.1 − 0.6 V *vs.* RHE, while the pure PANI shows electron transfer number around 2.48 and H$_2$O$_2$ selectivity around 76.3%. PANI/CDs−Co− 2 displays the highest H$_2$O$_2$ selectivity of nearly 100.0% at 0.2−0.5 V *vs.* RHE as shown in the shaded area inset Fig. 3d, indicating that ORR catalyzed by PANI/CDs−Co− 2 is almost dominated by 2e$^-$ pathway. PANI/CDs−Co− 1, PANI/CDs−Co− 3 and PANI/CDs−Co− 4 deliver the electron transfer number of 2.27, 2.43 and 2.57, respectively, and the corresponding selectivity of H$_2$O$_2$ are 86.3%, 78.3%, 71.6%. respectively. These results indicate that the selectivity of H$_2$O$_2$ by oxygen reduction catalyzed by PANI increased with the introduction of CDs−Co, reaching a peak when the amount of CDs−Co is 2 mg, but then decreases with the increase of CDs−Co. The chronoamperometry measurement was also employed to evaluate the long−term stability of PANI/CDs−Co− 2. As shown in Fig. 3e, during the 10 h test, the disk current and ring current of PANI/CDs−Co− 2 remain stable, and the selectivity of H$_2$O$_2$ remains basically unchanged. SEM and TEM were also employed to observed the morphology of PANI/ CDs−Co−2 after chronoamperometry tests, and no obvious change can be found (Fig. S9). The 2e$^-$ ORR performance of PANI/CDs−Co− 2 in 0.1 M KOH is also compared with other materials reported recently as shown in Fig. 3f and Table S1.

3.3. Electrochemical measurements in gas diffusion electrode (GDE)

Subsequently, the practical H$_2$O$_2$ productivity of PANI/CDs−Co− 2 was examined in a flow cell with a gas diffusion electrode as shown in Fig. 4a. The PANI/CDs−Co− 2 was sprayed on the gas diffusion layer (GDL) to obtain the cathode, and carbon paper was used as anode. Meanwhile, this anode and cathode were separated by anion exchange membrane (AEM). The mass transfer problem caused by the low concentration of dissolved oxygen can be effectively solved in this test system using GDL electrode. Fig. 4b displays the LSV tests carried on GDE in N$_2$ or O$_2$ atmosphere, where the LSV curves are significantly different, indicating that PANI/CDs−Co− 2 has significant catalytic capacity as a cathode catalyst rather than other electrochemical processes. We also tested current–time (I–t) curves at various voltages (0 −

0.7 V *vs.* RHE), as shown in Fig. 4c, and the current density at 0 V reached 85 mA cm^{-2}. Moreover, the yields of H$_2$O$_2$ and Faraday efficiency (FE) at these potentials were determined by potassium permanganate titration method. As shown in Fig. 4d, with the increase of overpotential, the yield of H$_2$O$_2$ increases rapidly, while the Faraday efficiency decreases slightly. PANI/CDs−Co− 2 exhibits a maximum H$_2$O$_2$ production rates of 3.5 mol g$_{cat}^{-1}$ h^{-1} at 0 V *vs.* RHE, while the faraday efficiency is about 86.5%. Meanwhile, the chronoamperometry curves of the PANI/CDs−Co− 2 and PANI/CDs assembled GDE were displayed in Fig. 4e. The GDE assembled by PANI/CDs−Co− 2 displays a slight attenuation after 10 h test, and its stability was better than GDE assembled by pure PANI. It is noteworthy that PANI/CDs−Co− 2 catalyst also shows higher H$_2$O$_2$ productivity than most of catalysts reported in recent years as shown in Fig. 4f and Table S2.

3.4. Pulse voltage-induced current (PVC) tests

The above electrochemical test results show that PANI/CDs−Co− 2 has excellent selectivity of 2e$^-$ ORR, but the electron transfer numbers of pure PANI and CDs−Co as components are 2.48 and 3.90, respectively. Therefore, it is worth of studying how the two components synergistically catalyze the 2e$^-$ pathway of ORR. During the electrocatalytic process, catalysts accelerate reactions by facilitating the needed electron transfer, which tends to be quite fast, and cause the breaking of chemical bonds and the formation of new ones. Here, pulse voltage-induced current (PVC) technology was used to study the ORR process driven by applied bias, by comparing potential and charge under different atmospheric conditions (for details, see Supplementary experimental section and Fig. S10). Fig. 5a shows section of the PVC protocol between anodic (0.90 V) and cathodic (0.59 V) non−iR corrected potentials (black line) and the corresponding current response (red line). And Fig. 5b shows the comparison of inverted cathodic current decay after background subtraction with the anodic current signal upon the reverse. The charge stored in the catalyst at different potential is quantified by integrating the current response to the cathodic voltage pulses and subtracting the oxygen reduction background. The charge stored by the catalyst is determined by the double layer capacitance and
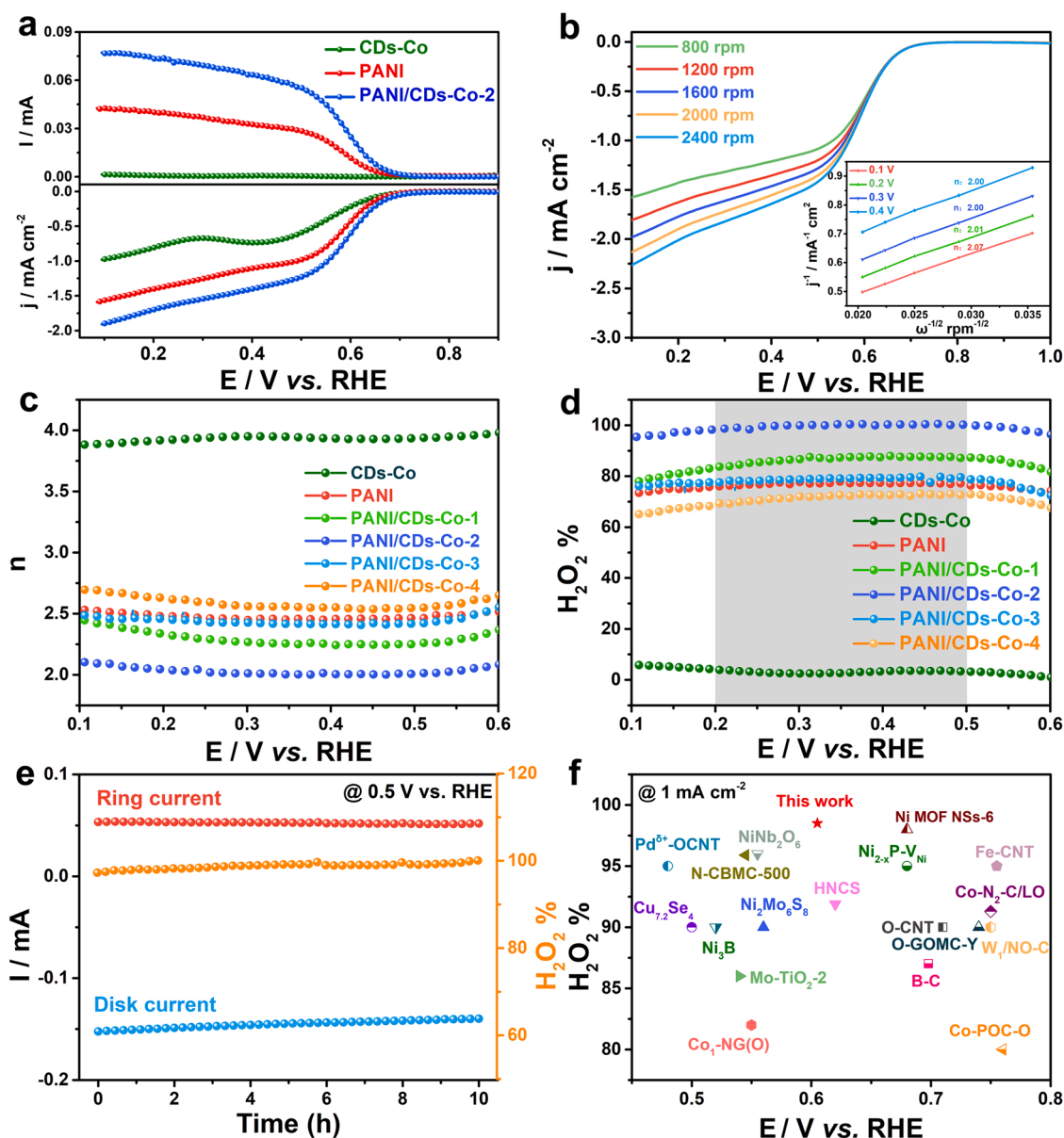
Fig. 3. Electrocatalytic 2e⁻ ORR performance. (a) LSV curves of CDs−Co, PANI and PANI/CDs−Co− 2. The bottom half part represents the disk current density, while the upper half part represents the ring current. (b) LSV curves at different at different rotational speeds and K–L plots of PANI/CDs−Co− 2 at different potentials. (c) The calculated electron transfer number. (d) The calculated H₂O₂ selectivity. (e) The chronoamperometry curve and corresponding H₂O₂ selectivity of the PANI/CDs−Co− 2 in 10 h. (f) The comparison 2e⁻ ORR performance of PANI/CDs−Co− 2 and recent reported electrocatalysts.

pseudo−capacitance of the material itself. As shown in Fig. 5c, the charge stored in the O₂ saturated electrolyte is significantly higher (0.0045 mC) than the charge stored in N₂ saturated electrolyte (0.0002 mC) by PANI/CD−Co− 2 at 0.81 V *vs.* RHE (Fig. S11). This is because O₂ molecules are adsorbed to the surface of PANI/CD−Co− 2, when bias is applied, electrons begin to transfer from the catalyst to the O₂ molecules, where the O₂ molecules act as dielectric and begin to store charge. Moreover, the capacitance *versus* potential plot of PANI and PANI/CDs−Co− 2 are shown in Fig. 5d. When the applied potential is larger than 0.67 V *vs.* RHE, no oxygen reduction reaction occurs on the surface of PANI/CDs−Co− 2 and the capacitance does not change significantly. When the applied potential is less than 0.67 V *vs.* RHE, the capacitance of PANI/CDs−Co− 2 increases significantly. At this time, the O₂ absorbed on the catalyst surface begins to undergo reduction reaction, and due to the increase of bias voltage, the O₂ molecule gains more charge, resulting in a larger capacitance. The voltage of 0.67 V *vs.* RHE was basically consistent with the ORR onset potential (0.68 V *vs.* RHE)

obtained by the above electrochemical test, indicating that O₂ molecules act the role of the dielectric when the voltage is higher than 0.67 V *vs.* RHE, and when the voltage is lower than 0.67 V *vs.* RHE, O₂ molecules begin to act as the active species involved in the reaction. Similarly, the O₂ molecules adsorbed by PANI begin to play different roles at the threshold of 0.63 V *vs.* RHE. It is worth noting that the overpotential required for oxygen molecules to be activated is significantly reduced after the introduction of CDs-Co. When the limiting current density is reached, oxygen adsorption and consumption reach a dynamic balance, and the capacitance value does not continue to increase. Roles of O₂ molecules at different overpotentials are shown in Fig. 5e. As the overpotential increases, the stronger the ability to charge the oxygen molecules, the more electron they stored, and when the critical potential for ORR is reached, the oxygen molecules begin to change from their role as a dielectric to a reactive species.
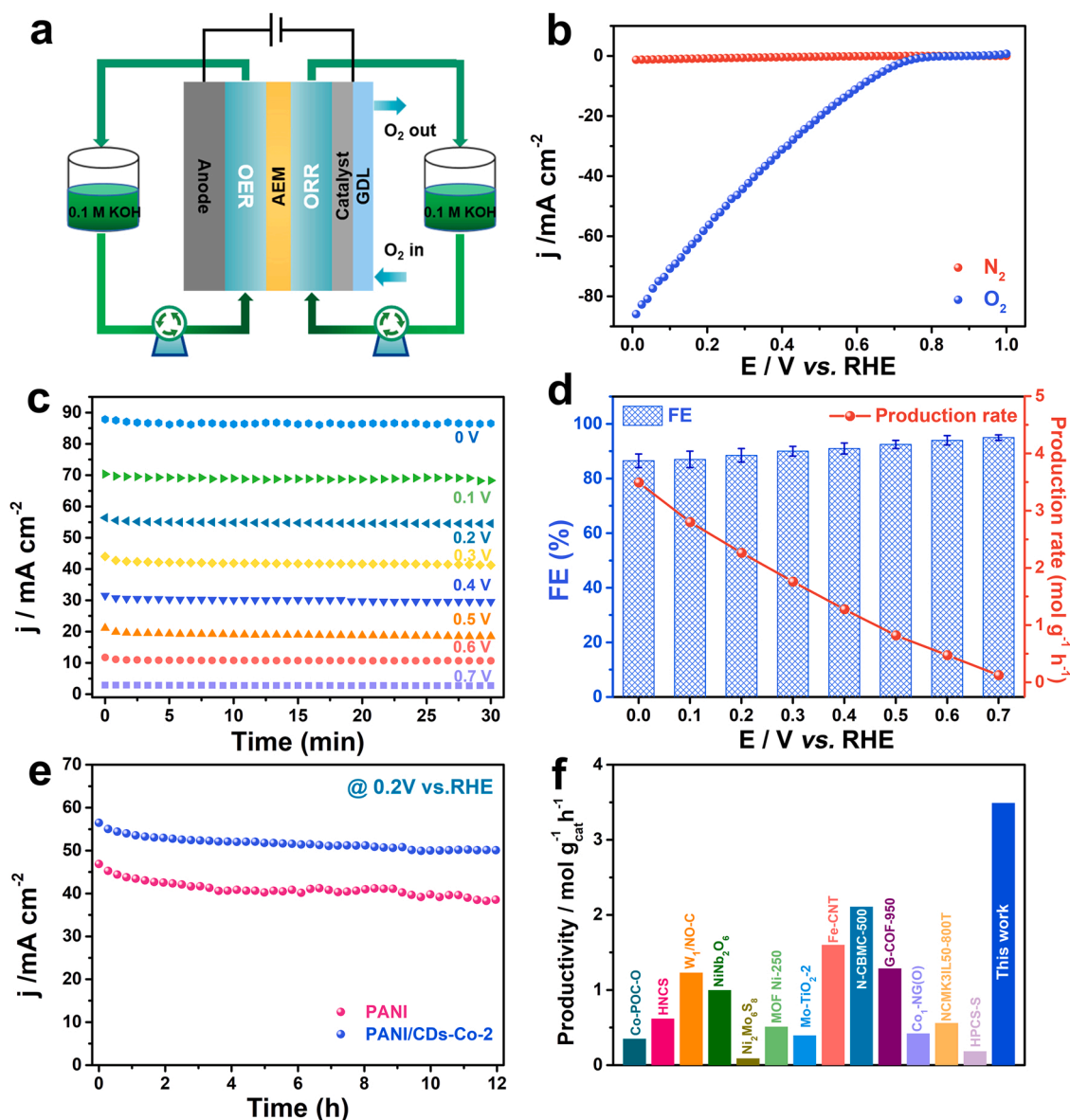
Fig. 4. Electrochemical tests in gas diffusion electrode (GDE). (a) The schematic diagram of flow cell electrolytic device. (b) LSV curves of PANI/CDs−Co− 2 in the O_2 and N_2 atmosphere. (c) I–t curves of PANI/CDs−Co− 2 at different potentials. (d) H_2O_2 faradaic efficiency (left) and production rates of H_2O_2 at various potentials (right) under the condition of entering O_2 (e) The I–t curves of PANI and PANI/CDs−Co− 2 under the condition of flow cell electrolytic device (@0.2 V *vs.* RHE). (f) Comparison of H_2O_2 productivity with recent reported catalysts.

3.5. Photo-induced voltage (TPV) tests and analysis

As shown in Fig. 6a, PANI is identified as an n − type semiconductor based on the positive slope in the Mott−Schottky plot, while CDs−Co is confirmed as a p − type semiconductor due to the negative slope in the Mott−Schottky plot (Fig. 6b). The Mott−Schottky plot in Fig. 6c shows an inverted "V−shape", indicating that p − n heterojunction existed in PANI/CDs−Co− 2 composite. The existence of an electric field in the charge region of the p − n heterojunction causes electrons to flow from PANI with high fermi level to CDs−Co with low Fermi level. In order to investigate the electron transfer behavior at the interface between PANI and CDs−Co, a transient photo−induced voltage (TPV) technology was employed to record the electron transport kinetics. Notably, Fig. 6d shows the typical TPV decay curves, where the signal of CDs−Co is completely opposite to PANI, because PANI and CDs−Co are n − type and p − type respectively, which is consistent with the results of Mott−Schottky plot. The time decay constant (τ) was calculated, which reflects the average electron relaxation time [49]. The lower τ value is,

the shorter the charge relaxation time is and the faster the charge transfer is. Among all samples, PANI shows the slowest decay rate, and the value of τ was calculated to be 0.235 ms. The τ of PANI/CDs−Co− 1, PANI/CDs−Co− 2, PANI/CDs−Co− 3, PANI/CDs−Co− 4 are 0.1941, 0.1874, 0.1489 and 0.1467 ms, respectively. With the increase of proportion of CDs−Co in the composite, the value of τ decreased gradually, indicating that faster charge transfer behavior is generated at the complex interface. Fig. 6e shows an enlarged image of the shaded area in Fig. 6a. It is noteworthy that with the introduction of CDs−Co, the decay curves of composites present a negative signal, which is due to the formation of p − n heterojunction between PANI and CDs−Co. As the content of CDs−Co increases, the area of negative signal increases. Besides, the decay time cannot fully reflect the charge transfer kinetics process, and the interfacial charges have different transfer rates, so it is necessary to further analyze the TPV decay curves. Based on the TPV decay curves, Fast Fourier Transform (FFT) was employed, which is a tool that breaks a waveform into an alternate representation, characterized by sine and cosines. As shown in Fig. 6f, there are no visible
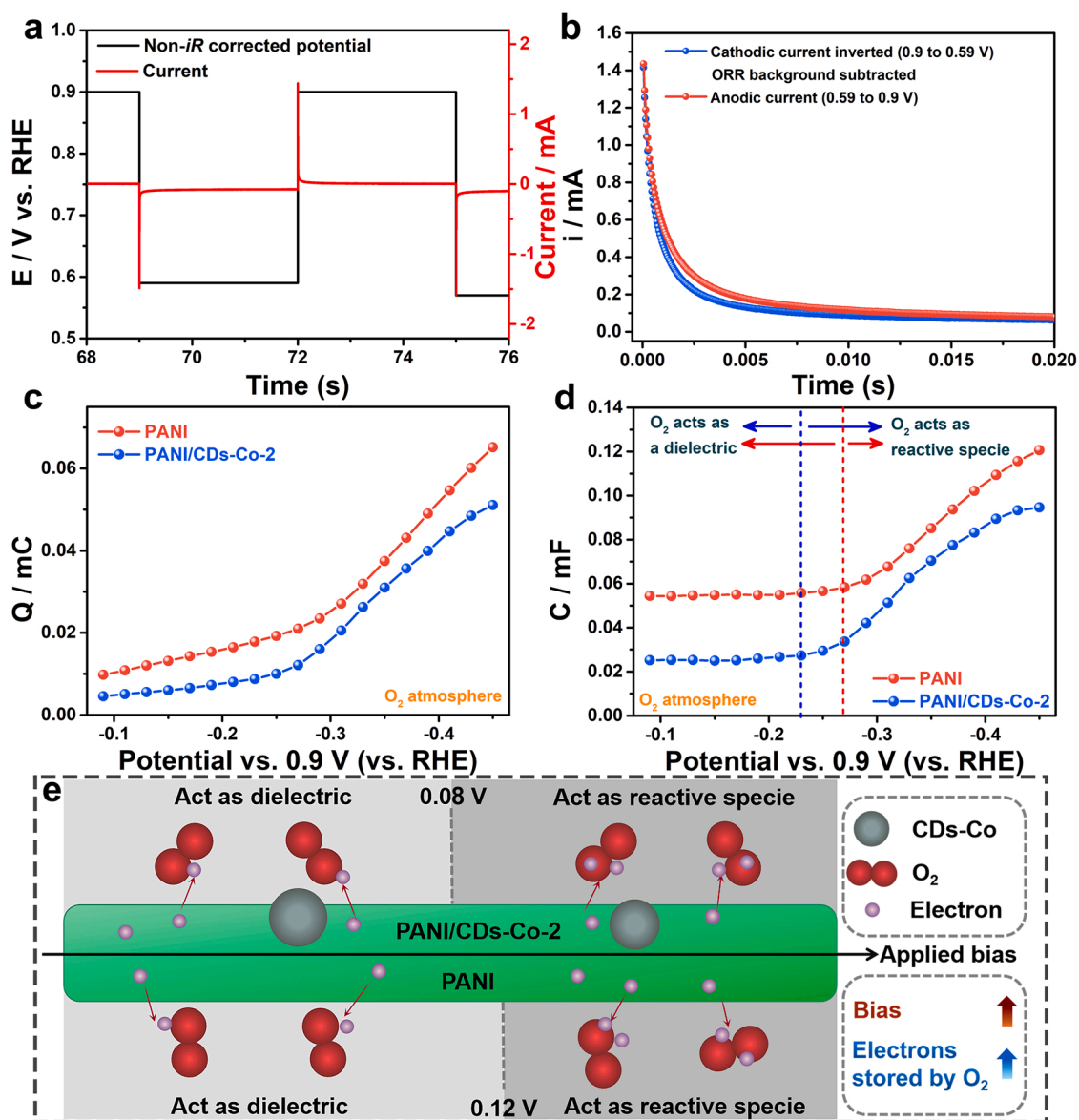
Fig. 5. Oxygen activation mechanism. (a) Section of the pulse voltammetry protocol (black) showing a reductive and oxidative pulse with the current response (red). (b) Inverted cathodic current decay after background subtraction (step from 0.9 V to 0.59 V) and the anodic current signal upon the reverse (0.59–0.9 V). Charge *versus* potential (c) and corresponding capacitance *versus* potential (d) from pulse voltammetry of PANI and PANI/CDs−Co− 2 in O_2 saturated 0.1 M KOH. (e) Schematic diagram of the role of O_2 molecules at different overpotentials. The potentials (0.08 V and 0.12 V) indicated are the over-potential relative to the equilibrium potential of $2e^-$ ORR in alkaline (0.75 V *vs.* RHE).

peaks in the FFT curves of all samples, indicating that there are no evident static or periodic frequency components. FFT can only recognize the frequency components of these signals, but it cannot distinguish when these frequency components occur [50]. Therefore, Continuous Wavelet transform (CWT) was used for further analysis, which is a frequency scale/time scale analysis method for non−static signals [51]. 2D CWT spectra of CDs−Co, PANI, PANI/CDs−Co− 1, PANI/CDs−Co− 2, PANI/CDs−Co− 3 and PANI/CDs−Co− 4 are shown in Fig. S12, and their corresponding 3D spectra are shown in Fig. S13. As can be seen in these spectra, the main frequency range of the signal of these samples is from 0.1 to 15 Hz, indicating that the interface electron transfer velocity distribution of the catalyst is relatively close. To further study the interface electron transfer kinetics, the peak positions of intensity−time curves of three samples at different frequency were compared. The smaller the frequency scale is, the slower the interfacial electron transfer process is, while the higher the frequency scale is, the faster the interfacial electron transfer process is. Therefore, we divided the frequency

scale in this work into three regions, including low frequency scale region (1 −5 Hz), medium frequency scale region (6 −10 Hz) and high frequency scale region (11 −15 Hz). At the low frequency scale (1 Hz) as shown in Fig. 6g, the time corresponding to the peak of PANI is the shortest (t_1 = 0.458 ms), implying the slowest interfacial electron transport on PANI. By contrast, PANI/CDs−Co− 1, PANI/CDs−Co− 2, PANI/CDs−Co− 3 and PANI/CDs−Co− 4 expend around t_2 = 0.4455 ms, t_3 = 0.4353 ms, t_4 = 0.4214 ms and t_5 = 0.4088 ms, respectively, to reach the peaks. We can observe that with the increase of CDs−Co, the peak position continues to move forward on the time scale, indicating that the electron transfer rate is accelerating. Moreover, when fixed at other low frequency scale (3 Hz, 5 Hz), similar results can also be obtained (Fig. S14). But the time gap is narrowing as shown in Table S3. In addition, there is almost no time difference in the middle frequency region (Figs. 6h and S15) and the high frequency region (Figs. 6i and S16). Since a p − n heterojunction is constructed between PANI and CDs−Co, electrons will transfer from PANI to CDs−Co when
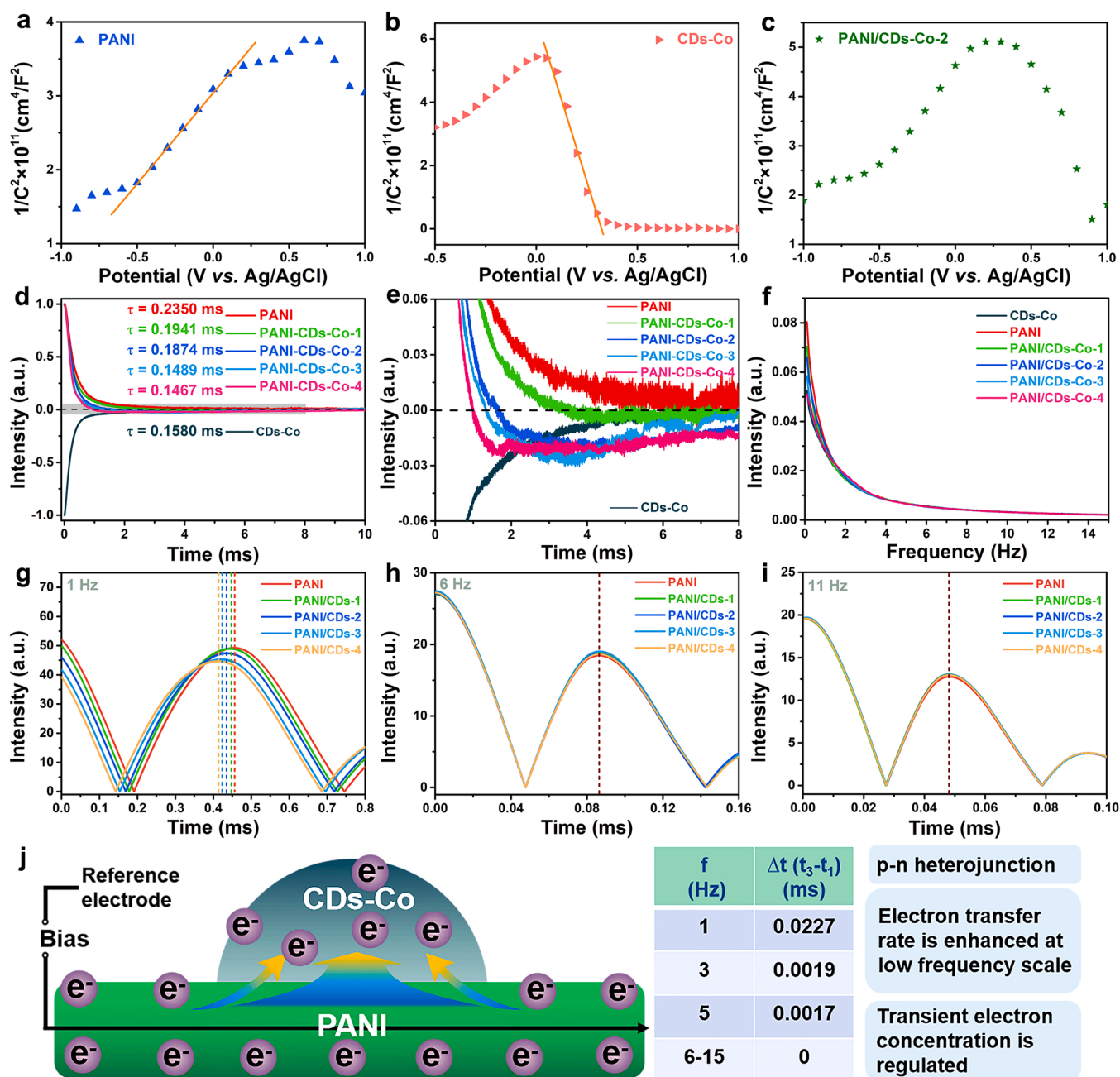
Fig. 6. Charge transfer mechanism. (a, b, c) The Mott−Schottky plots of PANI, CDs−Co and PANI/CDs−Co− 2, respectively. (d) TPV curves, (e) local detail image of TPV curves and (f) FFT curves of PANI, CDs−Co, PANI/CDs−Co− 1, PANI/CDs−Co− 2, PANI/CDs−Co− 3 and PANI/CDs−Co− 4. (g, h,i) The compared Intensity−Time curves at fixed frequency of 1 Hz, 6 Hz and 11 Hz. (j) Schematic diagram of CDs−Co regulating electron transfer behavior on PANI.

bias applied. These results indicate that the CDs−Co makes the slow interfacial electron transfer faster and has no obvious effect on the fast electron transfer process. Fig. 6j shows the schematic diagram of CDs−Co regulating electron transfer behavior on PANI. The more CDs−Co there are, the faster the electron is transferred from PANI to CDs−Co, resulting the lower instantaneous electron concentration on PANI. A lower instantaneous electron concentration is more beneficial for $2e^-$ ORR, since the O_2 molecules cannot receive sufficient electrons, resulting in the reaction that tends to be dominated by the $2e^-$ pathway [19,20]. Meanwhile, instantaneous electron concentration on CDs−Co increases, but the $4e^-$ ORR driven by CDs−Co is weak and can be ignored on the whole. However, when the content of CDs−Co is too large, the $4e^-$ on CDs−Co can not be ignored, and the overall selectivity of the composite will decrease, which is also consistent with the

electrocatalytic test results.

4. Conclusion

In this work, a series of PANI/CDs−Co heterojunctions were constructed to investigate the relationship between electrocatalytic kinetics and ORR selectivity. The PVC tests indicate that CDs−Co can effectively reduce the bias required for activation of oxygen molecules. The TPV technology shows that the electron transfer from PANI to CDs−Co, resulting the lower instantaneous electron concentration on PANI, which is conducive to the occurrence of $2e^-$ ORR. As a result, the PANI/CDs−Co− 2 shows a nearly 100% H_2O_2 selectivity, higher than that of 76.3% of PANI, and exhibits a H_2O_2 productivity of 3.5 mol g_{cat}^{-1} h^{-1} at 0 V *vs.* RHE tested by the GDE device. This work highlights the rational

design of multiphase nanostructures with heterojunction as efficient electrocatalysts for potential H_2O_2 production. Meanwhile, it also provides a new way to understand the kinetic process of electrocatalytic oxygen reduction reaction.

CRediT authorship contribution statement

Yunjie Zhou: Data curation, Visualization. **Xiaoqing Gu:** Investigation. **Jie Wu:** Formal analysis. **Hui Huang:** Writing – original draft, Project administration. **Mingwang Shao:** Software. **Yang Liu:** Resources, Writing – review & editing, Supervision. **Zhenhui Kang:** Conceptualization, Funding acquisition, Writing – review & editing, Supervision.

Declaration of Competing Interest

The authors declare that they have no known competing financial interests or personal relationships that could have appeared to influence the work reported in this paper.

Data availability

Data will be made available on request.

Acknowledgments

Appendix A. Supplementary material

Supplementary data associated with this article can be found in the online version at doi:10.1016/j.apcatb.2022.122105.

References

[1] X. Huang, W. Zhang, W. Liu, J. Zhang, M. Song, C. Zhang, J. Zhang, D. Wang, Nb$_2$CT$_x$ MXenes functionalized Co−NC enhancing electrochemical H_2O_2 production for organics degradation, Appl. Catal. B Environ. 317 (2022), 121737, https://doi.org/10.1016/j.apcatb.2022.121737.

[2] P. Su, M. Zhou, X. Lu, W. Yang, G. Ren, J. Cai, Electrochemical catalytic mechanism of N-doped graphene for enhanced H_2O_2 yield and in-situ degradation of organic pollutant, Appl. Catal. B Environ. 245 (2019) 583–595, https://doi.org/10.1016/j.apcatb.2018.12.075.

[3] C. Xia, Y. Xia, P. Zhu, L. Fan, H. Wang, Direct electrosynthesis of pure aqueous H_2O_2 solutions up to 20% by weight using a solid electrolyte, Science 366 (2019) 226–231, https://doi.org/10.1126/science.aay1844.

[4] C. Xia, J.Y. Kim, H. Wang, Recommended practice to report selectivity in electrochemical synthesis of H_2O_2, Nat. Catal. 3 (2020) 605–607, https://doi.org/10.1038/s41929-020-0486-1.

[5] X. Yang, Y. Zeng, W. Alnoush, Y. Hou, D. Higgins, G. Wu, Tuning two-electron oxygen-reduction pathways for H_2O_2 electrosynthesis via engineering atomically dispersed single metal site catalysts, Adv. Mater. (2022) 2107954, https://doi.org/10.1002/adma.202107954.

[6] Y. Ding, L. Xie, W. Zhou, F. Sun, J. Gao, C. Yang, G. Zhao, Y. Qin, J. Ma, Pulsed electrocatalysis enables the stabilization and activation of carbon-based catalysts towards H_2O_2 production, Appl. Catal. B Environ. 316 (2022), 121688, https://doi.org/10.1016/j.apcatb.2022.121688.

[7] J. Tang, T. Zhao, D. Solanki, X. Miao, W. Zhou, S. Hu, Selective hydrogen peroxide conversion tailored by surface, interface, and device engineering, Joule 5 (2021) 1432–1461, https://doi.org/10.1016/j.joule.2021.04.012.

[8] E. Pizzutilo, S.J. Freakley, S. Cherevko, S. Venkatesan, G.J. Hutchings, C. H. Liebscher, G. Dehm, K.J.J. Mayrhofer, Gold–palladium bimetallic catalyst stability: consequences for hydrogen peroxide selectivity, ACS Catal. 7 (2017) 5699–5705, https://doi.org/10.1021/acscatal.7b01447.

[9] S. Siahrostami, A. Verdaguer-Casadevall, M. Karamad, D. Deiana, P. Malacrida, B. Wickman, M. Escudero-Escribano, E.A. Paoli, R. Frydendal, T.W. Hansen, I. Chorkendorff, I.E.L. Stephens, J. Rossmeisl, Enabling direct H_2O_2 production through rational electrocatalyst design, Nat. Mater. 12 (2013) 1137–1143, https://doi.org/10.1038/nmat3795.

[10] X. Li, S. Tang, S. Dou, H.J. Fan, T.S. Choksi, X. Wang, Molecule confined isolated metal sites enable the electrocatalytic synthesis of hydrogen peroxide, Adv. Mater. (2021) 2104891, https://doi.org/10.1002/adma.202104891.

[11] E. Jung, H. Shin, B.-H. Lee, V. Efremov, S. Lee, H.S. Lee, J. Kim, W. Hooch Antink, S. Park, K.-S. Lee, S.-P. Cho, J.S. Yoo, Y.-E. Sung, T. Hyeon, Atomic-level tuning of Co–N–C catalyst for high-performance electrochemical H_2O_2 production, Nat. Mater. 19 (2020) 436–442, https://doi.org/10.1038/s41563-019-0571-5.

[12] K. Jiang, S. Back, A.J. Akey, C. Xia, Y. Hu, W. Liang, D. Schaak, E. Stavitski, J. K. Nørskov, S. Siahrostami, H. Wang, Highly selective oxygen reduction to hydrogen peroxide on transition metal single atom coordination, Nat. Commun. 10 (2019) 3997, https://doi.org/10.1038/s41467-019-11992-2.

[13] R. Shen, W. Chen, Q. Peng, S. Lu, L. Zheng, X. Cao, Y. Wang, W. Zhu, J. Zhang, Z. Zhuang, C. Chen, D. Wang, Y. Li, High-concentration single atomic Pt sites on hollow CuS$_x$ for selective O_2 reduction to H_2O_2 in acid solution, Chem 5 (2019) 2099–2110, https://doi.org/10.1016/j.chempr.2019.04.024.

[14] Z. Lu, G. Chen, S. Siahrostami, Z. Chen, K. Liu, J. Xie, L. Liao, T. Wu, D. Lin, Y. Liu, T.F. Jaramillo, J.K. Nørskov, Y. Cui, High-efficiency oxygen reduction to hydrogen peroxide catalysed by oxidized carbon materials, Nat. Catal. 1 (2018) 156–162, https://doi.org/10.1038/s41929-017-0017-x.

[15] Y. Xia, X. Zhao, C. Xia, Z.-Y. Wu, P. Zhu, J.Y. Kim, X. Bai, G. Gao, Y. Hu, J. Zhong, Y. Liu, H. Wang, Highly active and selective oxygen reduction to H_2O_2 on boron-doped carbon for high production rates, Nat. Commun. 12 (2021) 4225, https://doi.org/10.1038/s41467-021-24329-9.

[16] D. Iglesias, A. Giuliani, M. Melchionna, S. Marchesan, A. Criado, L. Nasi, M. Bevilacqua, C. Tavagnacco, F. Vizza, M. Prato, P. Fornasiero, N-doped graphitized carbon nanohorns as a forefront electrocatalyst in highly selective O_2 reduction to H_2O_2, Chem 4 (2018) 106–123, https://doi.org/10.1016/j.chempr.2017.10.013.

[17] Y. Jiang, P. Ni, C. Chen, Y. Lu, P. Yang, B. Kong, A. Fisher, X. Wang, Selective electrochemical H_2O_2 production through two-electron oxygen electrochemistry, Adv. Energy Mater. 8 (2018) 1801909, https://doi.org/10.1002/aenm.201801909.

[18] E. Jung, H. Shin, W. Hooch Antink, Y.-E. Sung, T. Hyeon, Recent advances in electrochemical oxygen reduction to H_2O_2: catalyst and cell design, ACS Energy Lett. 5 (2020) 1881–1892, https://doi.org/10.1021/acsenergylett.0c00812.

[19] J. Gao, B. Liu, Progress of electrochemical hydrogen peroxide synthesis over single atom catalysts, ACS Mater. Lett. 2 (2020) 1008–1024, https://doi.org/10.1021/acsmaterialslett.0c00189.

[20] J. Wu, Y. Han, X. Bai, X. Wang, Y. Zhou, W. Zhu, T. He, Y. Wang, H. Huang, Y. Liu, Z. Kang, The electron transport regulation in carbon dots/In$_2$O$_3$ electrocatalyst enable 100% selectivity for oxygen reduction to hydrogen peroxide, Adv. Funct. Mater. (2022) 2203647, https://doi.org/10.1002/adfm.202203647.

[21] Y. Wu, Y. Ding, X. Han, B. Li, Y. Wang, S. Dong, Q. Li, S. Dou, J. Sun, J. Sun, Modulating coordination environment of Fe single atoms for high-efficiency all-pH-tolerated H_2O_2 electrochemical production, Appl. Catal. B Environ. 315 (2022), 121578, https://doi.org/10.1016/j.apcatb.2022.121578.

[22] W. Liu, C. Zhang, J. Zhang, X. Huang, M. Song, J. Li, F. He, H. Yang, J. Zhang, D. Wang, Tuning the atomic configuration of Co-N-C electrocatalyst enables highly-selective H_2O_2 production in acidic media, Appl. Catal. B Environ. 310 (2022), 121312, https://doi.org/10.1016/j.apcatb.2022.121312.

[23] J. Zhao, C. Fu, K. Ye, Z. Liang, F. Jiang, S. Shen, X. Zhao, L. Ma, Z. Shadike, X. Wang, J. Zhang, K. Jiang, Manipulating the oxygen reduction reaction pathway on Pt-coordinated motifs, Nat. Commun. 13 (2022) 685, https://doi.org/10.1038/s41467-022-28346-0.

[24] C.H. Choi, H.C. Kwon, S. Yook, H. Shin, H. Kim, M. Choi, Hydrogen peroxide synthesis via enhanced two-electron oxygen reduction pathway on carbon-coated Pt surface, J. Phys. Chem. C 118 (2014) 30063–30070, https://doi.org/10.1021/jp5113894.

[25] C. Tang, L. Chen, H. Li, L. Li, Y. Jiao, Y. Zheng, H. Xu, K. Davey, S.-Z. Qiao, Tailoring acidic oxygen reduction selectivity on single-atom catalysts via modification of first and second coordination spheres, J. Am. Chem. Soc. 143 (2021) 7819–7827, https://doi.org/10.1021/jacs.1c03135.

[26] M. Melchionna, P. Fornasiero, High Pt single-atom density for high-rate generation of H_2O_2, Chem 5 (2019) 1927–1928, https://doi.org/10.1016/j.chempr.2019.07.005.

[27] Y. Zhou, H. Qi, J. Wu, H. Huang, Y. Liu, Z. Kang, Amino modified carbon dots with electron sink effect increase interface charge transfer rate of Cu-based electrocatalyst to enhance the CO_2 conversion selectivity to C_2H_4, Adv. Funct. Mater. (2022) 2113335, https://doi.org/10.1002/adfm.202113335.

[28] M. Han, S. Zhu, S. Lu, Y. Song, T. Feng, S. Tao, J. Liu, B. Yang, Recent progress on the photocatalysis of carbon dots: classification, mechanism and applications, Nano Today 19 (2018) 201–218, https://doi.org/10.1016/j.nantod.2018.02.008.

[29] Y. Wang, X. Liu, X. Han, R. Godin, J. Chen, W. Zhou, C. Jiang, J.F. Thompson, K. B. Mustafa, S.A. Shevlin, J.R. Durrant, Z. Guo, J. Tang, Unique hole-accepting carbon-dots promoting selective carbon dioxide reduction nearly 100% to methanol by pure water, Nat. Commun. 11 (2020) 2531, https://doi.org/10.1038/s41467-020-16227-3.

[30] Q. Niu, X. Gu, L. Li, Y. Zhang, G. Zhao, 3D CQDs-{001}TiO$_2$/Ti photoelectrode with dominant {001} facets: Efficient visible-light-driven photoelectrocatalytic oxidation of organic pollutants and mechanism insight, Appl. Catal. B Environ. 261 (2020), 118229, https://doi.org/10.1016/j.apcatb.2019.118229.

[31] M. Gu, D.-Y. Lee, J. Mun, D. Kim, H. Cho, B. Kim, W. Kim, G. Lee, B.-S. Kim, H. Kim, Solar-to-hydrogen peroxide conversion of photocatalytic carbon dots with anthraquinone: unveiling the dual role of surface functionalities, Appl. Catal. B Environ. 312 (2022), 121379, https://doi.org/10.1016/j.apcatb.2022.121379.

[32] Z. Liu, Z. Wang, S. Qing, N. Xue, S. Jia, L. Zhang, L. Li, N. Li, L. Shi, J. Chen, Improving methane selectivity of photo-induced CO$_2$ reduction on carbon dots through modification of nitrogen-containing groups and graphitization, Appl. Catal. B Environ. 232 (2018) 86–92, https://doi.org/10.1016/j.apcatb.2018.03.045.

[33] Y. Zhou, F. Yu, Z. Lang, H. Nie, Z. Wang, M. Shao, Y. Liu, H. Tan, Y. Li, Z. Kang, Carbon dots/PtW$_6$O$_{24}$ composite as efficient and stable electrocatalyst for hydrogen oxidation reaction in PEMFCs, Chem. Eng. J. 426 (2021), 130709, https://doi.org/10.1016/j.cej.2021.130709.

[34] Y. Zhao, Y. Liu, Z. Wang, Y. Ma, Y. Zhou, X. Shi, Q. Wu, X. Wang, M. Shao, H. Huang, Y. Liu, Z. Kang, Carbon nitride assisted 2D conductive metal-organic frameworks composite photocatalyst for efficient visible light-driven H$_2$O$_2$ production, Appl. Catal. B Environ. 289 (2021), 120035, https://doi.org/10.1016/j.apcatb.2021.120035.

[35] Z. Wu, X. Wang, Y. Li, H. Zhao, J. Wang, H. Huang, Y. Liu, Z. Kang, Converting water impurity in organic solvent into hydrogen and hydrogen peroxide by organic semiconductor photocatalyst, Appl. Catal. B Environ. 305 (2022), 121047, https://doi.org/10.1016/j.apcatb.2021.121047.

[36] J.-X. Feng, L.-X. Ding, S.-H. Ye, X.-J. He, H. Xu, Y.-X. Tong, G.-R. Li, Co(OH)$_2$@PANI hybrid nanosheets with 3D networks as high-performance electrocatalysts for hydrogen evolution reaction, Adv. Mater. 27 (2015) 7051–7057, https://doi.org/10.1002/adma.201503187.

[37] H. Xu, A.-L. Wang, Y.-X. Tong, G.-R. Li, Enhanced catalytic activity and stability of Pt/CeO$_2$/PANI hybrid hollow nanorod arrays for methanol electro-oxidation, ACS Catal. 6 (2016) 5198–5206, https://doi.org/10.1021/acscatal.6b01010.

[38] J.-X. Feng, S.-Y. Tong, Y.-X. Tong, G.-R. Li, Pt-like hydrogen evolution electrocatalysis on PANI/CoP hybrid nanowires by weakening the shackles of hydrogen ions on the surfaces of catalysts, J. Am. Chem. Soc. 140 (2018) 5118–5126, https://doi.org/10.1021/jacs.7b12968.

[39] S. Jia, Q. Zhu, M. Chu, S. Han, R. Feng, J. Zhai, W. Xia, M. He, H. Wu, B. Han, Hierarchical metal–polymer hybrids for enhanced CO2 electroreduction, Angew. Chem. Int. Ed. (2021) 10977–10982, https://doi.org/10.1002/anie.202102193.

[40] M.R. Haider, W.-L. Jiang, J.-L. Han, H.M.A. Sharif, Y.-C. Ding, H.-Y. Cheng, A.-J. Wang, In-situ electrode fabrication from polyaniline derived N-doped carbon nanofibers for metal-free electro-Fenton degradation of organic contaminants, Appl. Catal. B Environ. 256 (2019), 117774, https://doi.org/10.1016/j.apcatb.2019.117774.

[41] R. Silva, D. Voiry, M. Chhowalla, T. Asefa, Efficient metal-free electrocatalysts for oxygen reduction: polyaniline-derived N- and O-doped mesoporous carbons, J. Am. Chem. Soc. 135 (2013) 7823–7826, https://doi.org/10.1021/ja402450a.

[42] J. Hu, S.-S. Li, J.-F. Li, Y.-L. Wang, X.-Y. Zhang, J.-B. Chen, S.-Q. Li, L.-N. Gu, P. Chen, Surface functionalization of polyaniline and excellent electrocatalytic performance for oxygen reduction to produce hydrogen peroxide, Chem. Eng. J. 431 (2022), 133921, https://doi.org/10.1016/j.cej.2021.133921.

[43] Y. Zhou, Y. Sun, C. Zhu, Y. Liu, X. Dai, J. Zhong, Q. Chen, H. Tian, R. Zhou, Z. Kang, C–O$^-$–K$^+$(Na$^+$) groups in non-doped carbon as active sites for the oxygen reduction reaction, J. Mater. Chem. A 6 (2018) 8955–8961, https://doi.org/10.1039/C8TA02445F.

[44] M. Li, C. Han, Y. Zhang, X. Bo, L. Guo, Facile synthesis of ultrafine Co$_3$O$_4$ nanocrystals embedded carbon matrices with specific skeletal structures as efficient non-enzymatic glucose sensors, Anal. Chim. Acta 861 (2015) 25–35, https://doi.org/10.1016/j.aca.2014.12.030.

[45] W. Shi, F. Guo, M. Li, Y. Shi, M. Shi, C. Yan, Constructing 3D sub-micrometer CoO octahedrons packed with layered MoS$_2$ shell for boosting photocatalytic overall water splitting activity, Appl. Surf. Sci. 473 (2019) 928–933, https://doi.org/10.1016/j.apsusc.2018.12.247.

[46] L. Huang, Y. Su, R. Qi, D. Dang, Y. Qin, S. Xi, S. Zaman, B. You, S. Ding, B.Y. Xia, Boosting oxygen reduction via integrated construction and synergistic catalysis of porous platinum alloy and defective graphitic carbon, Angew. Chem. Int. Ed. 60 (2021) 25530–25537, https://doi.org/10.1002/anie.202111426.

[47] G. Nascimento, X-ray absorption spectroscopy of nanostructured polyanilines, Chem. Pap. 67 (2013) 933–945, https://doi.org/10.2478/s11696-013-0344-6.

[48] F.A. Permatasari, A.H. Aimon, F. Iskandar, T. Ogi, K. Okuyama, Role of C–N configurations in the photoluminescence of graphene quantum dots synthesized by a hydrothermal route, Sci. Rep. 6 (2016) 21042, https://doi.org/10.1038/srep21042.

[49] J. Wu, Y. Zhou, H. Nie, K. Wei, H. Huang, F. Liao, Y. Liu, M. Shao, Z. Kang, Carbon dots regulate the interface electron transfer and catalytic kinetics of Pt-based alloys catalyst for highly efficient hydrogen oxidation, J. Energy Chem. 66 (2022) 61–67, https://doi.org/10.1016/j.jechem.2021.07.012.

[50] Y. Liu, Y. Zhao, Q. Wu, X. Wang, H. Nie, Y. Zhou, H. Huang, M. Shao, Y. Liu, Z. Kang, Charge storage of carbon dot enhances photo-production of H$_2$ and H$_2$O$_2$ over Ni$_2$P/carbon dot catalyst under normal pressure, Chem. Eng. J. 409 (2021), 128184, https://doi.org/10.1016/j.cej.2020.128184.

[51] S. Dahlke, A. Kunoth, Biorthogonal wavelets and multigrid, in: W. Hackbusch, G. Wittum (Eds.), Adaptive Methods — Algorithms, Theory and Applications, Vieweg+Teubner Verlag, Wiesbaden, 1994, pp. 99–119, https://doi.org/10.1007/978-3-663-14246-1_7.